The Thesis Committee for Suyeong Jang Certifies that this is the approved version of the following Thesis:

Near infrared to visible intersubband transitions in all-oxide quantum wells using $BaSnO_3$

APPROVED BY
SUPERVISING COMMITTEE:

Alexander A. Demkov, Supervisor

Keji Lai, Co Supervisor

Near infrared to visible intersubband transitions in all-oxide quantum wells using $BaSnO_3$

by

Suyeong Jang

Thesis

Presented to the Faculty of the Graduate School of

The University of Texas at Austin

in Partial Fulfillment

of the Requirements

for the Degree of

Master of Arts

The University of Texas at Austin

December 2023

Acknowledgements

I would like to thank Dr. Demkov and his group for all their support and help. Dr. Demkov supervised me for 4 years and he always seemed very excited about our research, and I appreciated his eagerness, availability, support and his help throughout the year. Especially Agham helped me out immensely in regard to the experiment and answered so many of my questions in emails and in person and I appreciated his kindness and dedication to help. I would also like to thank Dr. Keji Lai for helping with the master's thesis. I would like to thank my family for being my constant support and inspiration for me. I especially want to thank my mom for always been very supportive of me and always giving me great life advice and being an awesome example for me to follow. I really appreciated my boyfriend Oleksiy for being my biggest support and help throughout graduate school. I can't thank him enough for all his love and kindness he's shown which inspired me to do everything I wanted to do.

Abstract

Near infrared to visible intersubband transitions in all-oxide quantum wells using $BaSnO_3$

Suyeong Jang, M.A.

The University of Texas at Austin, 2023

Supervisor: Alexander Demkov, Keji Lai

Quantum wells (QWs) are made up of a larger bandgap "barrier" material sandwiching the smaller bandgap "well" material. Recently, quantum well structures using metal oxides such as $SrTiO_3(STO)/LaAlO_3$ have been reported. They boast a rather large conduction band offset of ~2.3eV but suffer from large effective mass of STO (used as their "well" material). On the other hand, $BaSnO_3$ has a small effective mass of $m^*_{BSO} = 0.2m_e$ that allows for larger spacing of the QW energy levels. $BaSnO_3$ also, has very high mobility ($150 cm^2(Vs)^{-1}$) and a wide bandgap (~3.1eV) making it a great candidate in applications calling for transparent conductive films. We will discuss MBE-grown $Al_2O_3/BaSnO_3$ quantum wells demonstrating a high level of confinement. We have grown different thickness of our BSO layer and performed many characterizations on our quantum well such as XRD, XRR, RHEED, XPS, and ellipsometry measurement. The quantum wells in this thesis can allow intersubband transitions from visible to infrared range enabling many applications.

Table of Contents

List of Figures

1. INTRODUCTION

Chapter 1.1: Molecular Beam Epitaxy

Molecular beam Epitaxy (MBE) is a technique to grow high quality thin films in an ultra-high vacuum ($8 \times 10^{-8} - 8 \times 10^{-13}$Torr) environment. The basic MBE technique was developed by Alfred Y. Cho and John R. Arthur, Jr at Bell Laboratories in 1968. MBE has a very slow deposition rate (nanometers per minute), which allows for very high control over the stoichiometry and the thickness of the grown film, which is optimal for growing high quality crystals or quantum wells. In this thesis, I have used molecular beam epitaxy chamber at the Materials Physics Laboratory at UT Austin which has components such as the vacuum pumping system, water cooling system, effusion cells, e-beam evaporator, plasma source for oxygen, and RHEED system to monitor the crystallinity during the growth. I have included a photograph of the MBE chamber with the labeled parts in Figure 1.

Before the thin film growth takes place, the substrate is cleaned ultrasonically and with UV treatment. The substrate is then fastened on to the substrate holder and attached to the manipulator shaft. The sample can be heated radiatively from the coil placed above the sample. The coil is made of silicon carbide and heated from DC current, and the thermocouple wire in contact with the heater reads out the temperature.

During the film growth phase, the elemental sources are evaporated from the effusion cell or electron beam creating molecular beam which has a long mean free path of the molecules (larger than the source to substrate distance) due to the ultra-high vacuum environment. The mean free path of the particles can be described with the ideal gas law equation $\lambda = \frac{k_B T}{\sqrt{2}\pi d^2 p}$, where k_B is the Boltzmann constant, T is the temperature in Kelvin, p is the pressure of the gas

and d is the effective diameter of a particle. Effusion cell consists of high melting temperature material which is surrounded by heating coil. Effusion cells also have a water cooling to prevent the rest of MBE chamber from getting hot. Each effusion cell houses one elemental or compound source and is made up of a crucible made of heat resistant material. The effusion cells have a shutter that can close and open to control the elements that are being deposited on the substrate. Whenever we have materials that have a high melting temperature, we use the electron beam evaporator instead of the effusion cells. Electron beam evaporator has a high energy beam of electrons that are accelerated by high voltage. The high energy beam of electrons causes the atoms form the target to become gas, then they precipitate into solid form as they land on the substrate. The deposition rate of the material is measured by a quartz crystal microbalance (QCM), which measures the mass variation per unit area of the deposited film by measuring the change in the frequency of the quartz crystal resonator. The QCM can be moved manually into the molecular beam before the deposition to measure the flux of certain molecules.

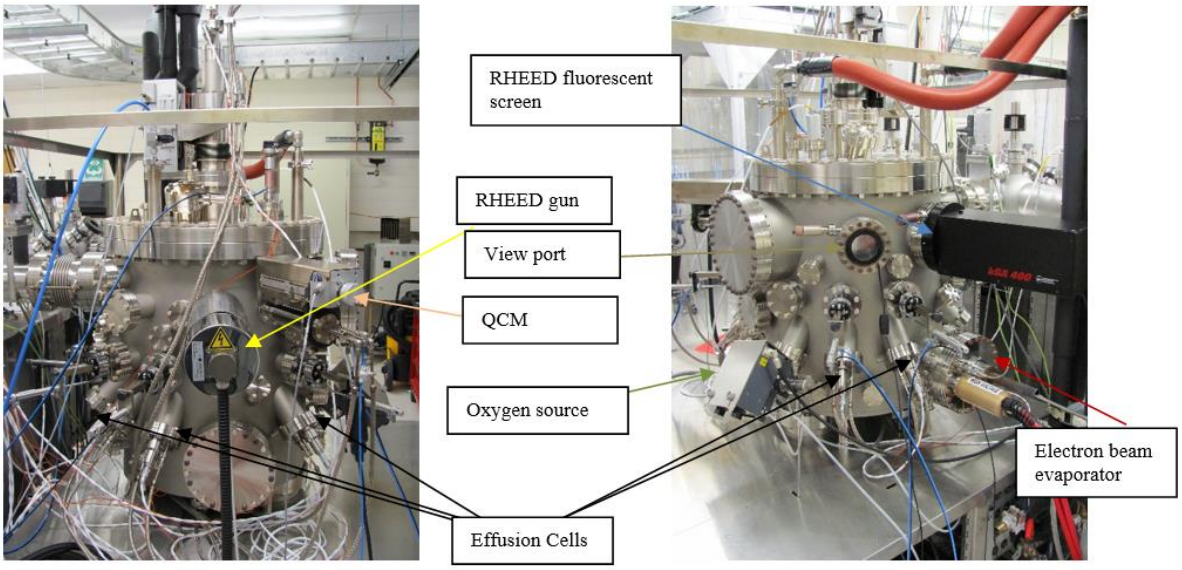

Figure 1: Picture of the Molecular Beam Epitaxy(MBE) system in the University of Texas at Austin. Different components are labeled in the image.

Chapter 1.2: Reflection High Energy Electron Diffraction (RHEED)

Reflection high-energy electron diffraction (RHEED) is a method developed to monitor in real time the thin film growth. RHEED is a surface sensitive electron diffraction technique used to monitor the thin film's crystallinity, and surface roughness. The high energy electron beam (energy of 10-100keV) gets projected from the electron gun and diffracts from the sample surface at a very small incidence angle ($1° - 4°$) and impinge on the phosphor fluorescence screen creating specific diffraction patterns according to the surface features of the sample. The CCD camera from the outside records the image. The electrons penetrate only a few Angstroms into the sample, so RHEED tells us information about the surface of the film.

The Ewald spere is a geometric construction used in electron diffraction which helps us understand and visualize the diffraction pattern (Figure 2). We assume that there is elastic scattering (no change in energy after diffraction), we know that the magnitude of the incident wavevector k_0 has to be same as the outgoing wavevectors k_1 and k_2. ($|k_0| = |k_1| = |k_2|$) This means that the wavevectors must all lie on the Ewald spere with the radius $|k_0|$. Since the crystal can be described as lattice of atoms, the Fourier transform of this is a reciprocal lattice where at the position of every atom, we have a set of vertical lines or rods which can be seen in Figure 2. The intersection between these reciprocal lattice rods and the Ewald sphere gives a series of concentric circles, called Laue zone, which are observed on our fluorescence screen. The smallest circle is called the 0^{th} Laue zone (L_0) and the second smallest circle is called 1^{st} Laue zone(L_1). The Ewald sphere has a radius of $r_e = 2\pi/\lambda$, where λ is the wavelength of electrons accelerated through a voltage V. The spacing of the RHEED streaks on the fluorescent screen is

given by the Bragg scattering condition $D = \lambda L/d$ where λ is wavelength of the incoming electron, d is the spacing of the atomic planes of the crystal and L is the distance between the crystal and the screen.

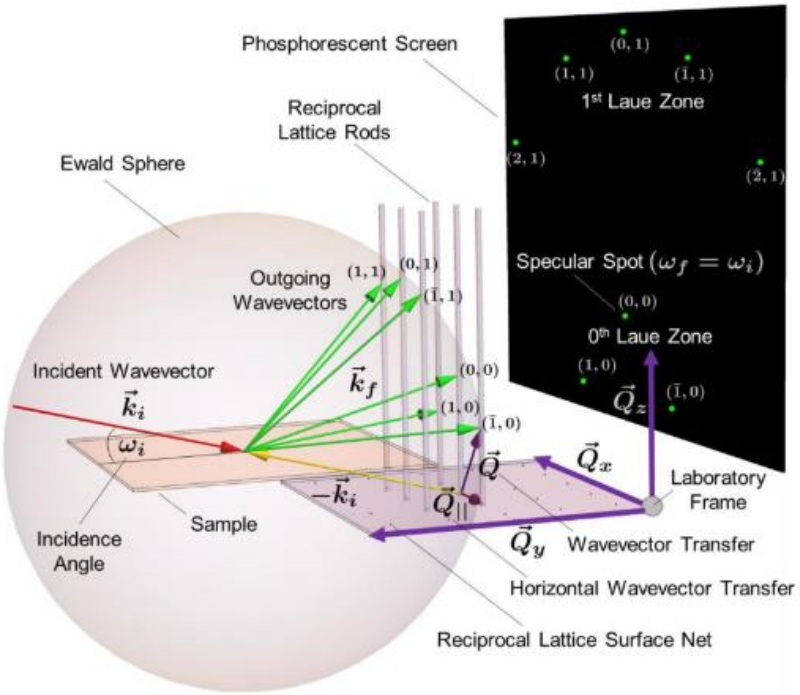

Figure 2: Picture of the Ewald Sphere construction with the incident wavevector k_i and the outgoing wavevectors k_f. The highly energetic electrons hit the sample at a small incidence angle (1°-3°) and the diffraction pattern forms from the phosphorescent screen. The intersection between the reciprocal rods and the Ewald Sphere is what we will see a diffraction pattern.[1]

The spatial resolution of the RHEED is determined by the coherence length of the electron beam, which has equation $l = \frac{\lambda}{\sqrt{2(\Delta\theta)^2 \sin^2\alpha + \left(\frac{\Delta E}{E}\right)^2 \cos^2\alpha}}$, where λ is the wavelength of

the electron wave and α is the angle between the incident wave, l is the coherence length, ΔE is the energy spread of the electron and $\Delta\theta$ is the divergence angle.

The shape of the RHEED pattern depends on the sample surface morphology, which is shown in Figure 3. When the sample has an atomically flat surface and perfect single crystalline structure, the reciprocal rods are very sharp and has same intensity for all rods (Figure 3a). This is because 2D lattice from real space would result in sharp, infinitely long rods that are extending perpendicular to the lattice plane in reciprocal space. In RHEED image, we would see diffraction spots that are on the Laue zone and has same intensities. Since actual samples are not always ideal and they can have uneven surface or be polycrystalline, the RHEED patterns can differ due to such imperfections of the samples. In real life, we also have electrons that are penetrating several atomic layers below the surface, so the reciprocal rods have different intensities due to the interferences between the waves from different layers. When we have a finite size domain with a small out of phase domain (Figure 3b), then we would have wider reciprocal rods and the width that scales inversely with the domain size. When the wide rod intersects with Ewald sphere, it produces elongated ellipse or streaks. This is often what we see for epitaxial growth of typical films. For the cases where surface has terraces (Figure 3c) with one-atomic height difference, the electron waves interfere from the terraces interface and create a reciprocal rod that has intensity modulations due to interferences and is accompanied by another reciprocal rods produced by the terrace with different height. In RHEED image, it produces diffraction pattern that has satellite spots and streaks. The rods are narrow, because each terrace is flat locally. When the surface has many terraces of different height, the different terrace interface interacts with each other and sometimes become sharp or wide depending on whether the interference between the stepped surfaces is destructive or constructive and whether electron “see” one

surface due to interference or see all the stepped surfaces. This results in a long rod that has width modulation, and the RHEED pattern would be modulated streaks. Polycrystalline material has Laue rings and amorphous materials does not show a diffraction pattern and has a hazy background.

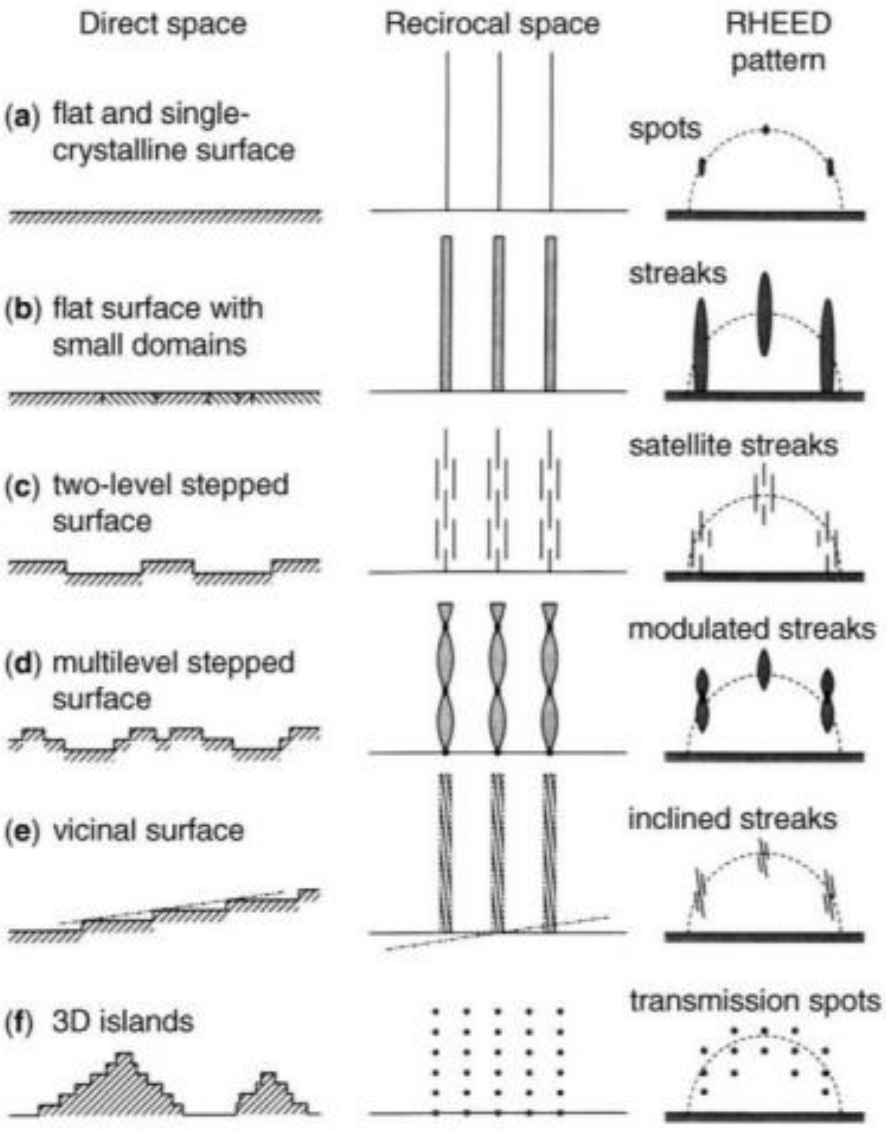
Direct space
Recirocal space
RHEED pattern
(a) flat and single-crystalline surface
spots
(b) flat surface with small domains
streaks
(c) two-level stepped surface
satellite streaks
(d) multilevel stepped surface
modulated streaks
(e) vicinal surface
inclined streaks
(f) 3D islands
transmission spots

Figure 3: Relationship between the real space morphology of the surfaces and the RHEED patterns. On the left, we have a direct space surface morphology shown, on the middle, we have corresponding reciprocal rods shown from the reciprocal space, and on the right, we show the corresponding RHEED images we would see. For the flat surface, we would have very thin rods that would intersect with the Ewald Sphere producing diffraction spots for the single crystalline surface(a) and streaks for surface with small domains(b). For the stepped surfaces, there will be constructive and destructive interferences which result in pattern such as (c)-(f) [2]

Chapter 1.3: Ellipsometry

Ellipsometry measures the change in polarization as light is reflected or transmitted from the surface of the film. The parameters that we measure are Δ (phase difference) and Ψ(amplitude ratio). This change in polarization can give us information about the film thickness, optical constants, roughness, crystallinity, and other material properties. We use a light source and polarize the light using a polarizer; after light is reflected off the sample, it goes through the polarization analyzer and detector to find the change of polarization. The change in polarization is commonly expressed as $\rho = \tan(\Psi)\, e^{i\Delta}$. The initial light is polarized so that the polarizer axis is oriented between the p- and s- planes and when the light gets reflected, it becomes elliptically polarized (hence the name "ellipsometer"). We can see the light polarization in Figure 4.

Using the changes in light polarization, we can find the material's properties such as film thickness and optical constants indirectly. After the sample's polarization is measured, we construct a model to describe the sample. Then we compare the experimental data and the calculated values. The unknown material properties can vary to reduce the difference between the experimental and calculated values. Mean Squared Error (MSE) could tell us how good our model is. The best answer is when MSE becomes the lowest value. At each wavelength, the ellipsometer

gives two data points, ψ and Δ, so in order to measure the optical constant (as is the case for my experiment) we should know the thickness of the sample and fix that parameter.

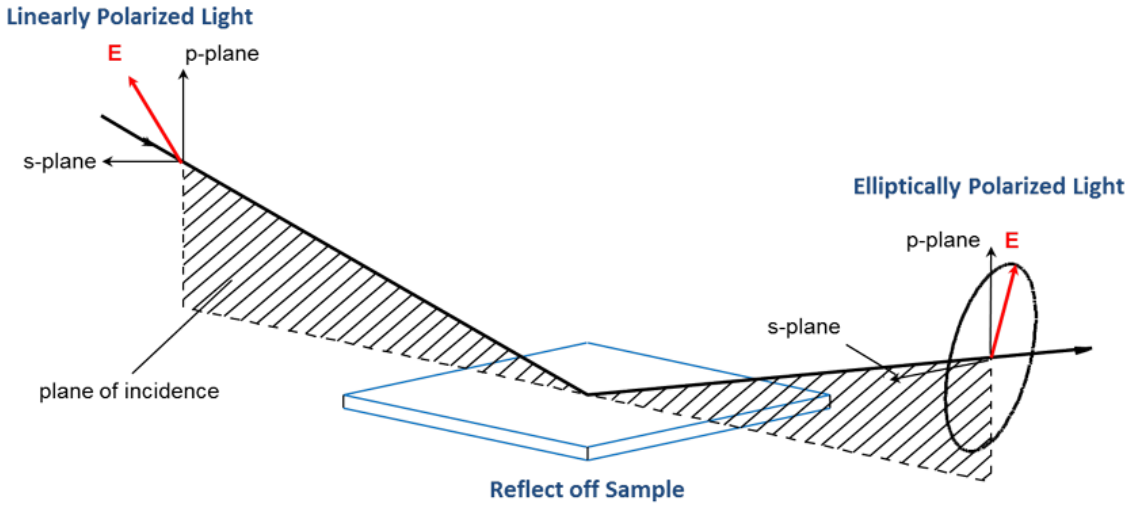

Figure 4: Schematic illustrating how the ellipsometer works. Linearly polarized light that has component in both p and s-plane reflects off the sample than becomes elliptically polarized and the change in polarization gets analyzed.[3]

Chapter 1.4: Quantum Wells

Esaki and Tsu first developed the semiconductor quantum well in 1970 and a lot of research has been done studying the interesting properties and physics of the quantum well system as well as developing quantum well devices. Fabricating quantum well devices require a very high level of control over the growth and high purity growth with few defects. Therefore, one uses molecular beam epitaxy (MBE) or chemical vapor deposition (CVD) that have control of the layer thickness down to a monolayer.

Quantum wells are a special type of heterostructures that are created by sandwiching the "well material" with two wider bandgap material regions called the "barrier". Both electrons and

holes see the lower energy in the quantum well and are confined in the thin well layer in the direction of growth. Quantum wells have applications in lasers, photodetectors, switches, and modulators.

One can also have periodic heterostructures of alternating materials of different bandgaps that form a superlattice. The superlattice has barriers that are thin enough to let the particles tunnel through and when the barriers are too thick, we call it a multiple quantum well structure. Common uses of multiple quantum well structures is in quantum cascade lasers and terahertz devices.

In a quantum well, the particles can still move freely in the direction parallel to the layers but is confined in the direction of the growth which we call the ***z*** direction. In order for the energy levels to be quantized, the well has to be very thin (comparable to the de Broglie wavelength of the particle which is given by $\lambda = \frac{h}{p}$), typically about 100 Å. We can understand the quantum well through the Schrodinger equation for an electron or a hole $-\frac{\hbar^2}{2m^*}\frac{d^2\phi_n}{dz^2} + V(z)\phi_n = E_n\phi_n$, where the E_n and ϕ_n are nth eigen energy and wavefunction respectively, m* is the effective mass of the particle, and $V(z)$ is the confining potential seen by the particle.

For the simplest case, the infinite well will have infinitely high barriers on either side and zero potential in the well. The solutions for the infinite quantum well energies are $E_n = -\frac{\hbar^2}{2m} * \left[\frac{n\pi}{L_z}\right]^2$, $n = 1,2,3 \ldots \phi_n = \sqrt{\frac{2}{L_z}}\sin(\frac{n\pi z}{L_z})$. Here, the L_z is the well width. For the finite quantum well with the finite height of the barrier, we can have "tunneling" across the barrier, and we should make sure that the wavefunctions and their slopes are continuous at the boundary. The Schrodinger equation for the particle in a finite quantum well is $-\frac{\hbar^2}{2m_b^*} * \frac{\partial^2\psi(z)}{\partial z^2} + V_0\psi(z) =$

$E\psi(z)$ where V_0 is the potential in the barrier regions. For the finite quantum well, there is a possibility that the particle can be found outside of the well (quantum tunneling) and the wavefunction decays exponentially across the barrier. A finite quantum well still does closely follow the $E \propto \frac{1}{L^2}$ energy trend. Since the energy of the level depends on the width of the quantum well, we can tune energy levels by changing the width of the quantum well. However, whenever we are fabricating the quantum well using epitaxy, there is a limit to how narrow we can make the quantum well with it still having a week defined structure. Usually is is a few unit cells. This can limit the tunability of the energy levels.

There have been many different materials used to make quantum wells such as $LaAlO_3/SrTiO_3$ and AlGaAs/GaAs. The potential well is understood as a conduction band profile across the heterostructure in the direction of stacking or the ***z*** direction. One of the important restrictions in choosing the well and barrier materials is that their lattice constants must be very similar, otherwise, it might be hard to grow "epitaxial" layers due to strain. The level of confinement also depends on the well depth, that for the electrons is controlled by the conduction band offset between the materials used to build the well. Most conventional semiconductors have less than 1.0 eV of the conduction band offset, which limits the separation between the energy levels of the quantum well and in turn the operating wavelength range of the laser or the diode. This is why we decided to fabricate quantum wells using wide bandgap oxide materials such and $BaSnO_3$ (BSO) as our "well material." The conduction band offsets between the oxides can be quite large and therefore, the tunability is very high if the effective mass is sufficiently low as is the case with BSO.

Chapter 1.5: Barium Stannate ($BaSnO_3$)

In this thesis, we will focus on fabricating the stannate based quantum well. Stannate materials such as $BaSnO_3$(BSO) and $SrSnO_3$(SSO) are of great interest for the potential Transparent Conductive Films (TCF) and high-speed electronics due to their wide bandgap and relatively high electric conductivity. Transparent conductive films are thin films of optically transparent and electronically conductive materials that are the important components in modern day electronic devices. So far, indium tin oxide (ITO) has been widely used as a TCF material, but since indium is scarce and costly, BSO is a great alternative that can replace ITO. Transparent conducting materials are often used in organic light-emitting diodes or OLEDs, touchscreens, and in solar energy applications. $BaSnO_3$ has a high n-type mobility when it is doped with lanthanum. La-doped $BaSnO_3$ bulk material has high electron mobility of $320 cm^2 V^{-1} s^{-1}$, which is the highest room temperature electron mobility among all perovskite oxides. The La-doped BSO thin film has a lower electron mobility than the bulk material, because of the crystalline defects and lattice mismatch between the BSO and the substrate.

Wide band gap semiconductors such as BSO can have applications in high-temperature and high-power electronics because the large bandgap allows them to operate at high voltage and temperature beyond what isa possible with conventional semiconductors.

$BaSnO_3$ has a cubic perovskite crystal structure with five atoms in the primitive unit cell and is shown in Figure 5.

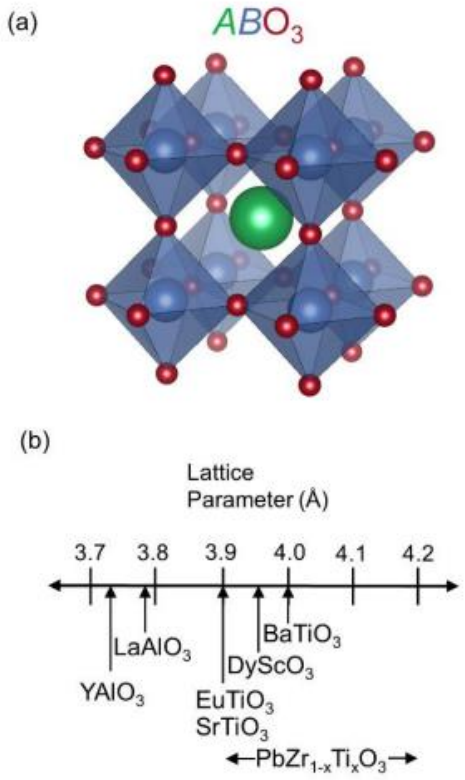

Figure 5: (a) Representation of the cubic crystal structure of ABO_3 perovskites where the green sphere represents A-site cations, blue spheres represent B-site cation and red sphere represents oxygen. For stannate the B site cation is Sn [4] (b) Lattice parameter of common ABO_3 perovskite materials. BSO has bulk lattice constant of 4.116Å which is little bigger than that if $BaTiO_3$.

2. DESIGN OF $BaSnO_3/SrTiO_3/Al_2O_3$ QUANTUM WELL

Both $BaSnO_3$ and $SrSnO_3$ have attracted significant interest in the area of transparent conductive oxides as they have large electron mobility and wide optical band gaps. Here, we propose an advanced quantum well structure design of $BaSnO_3$/STO/Al_2O_3 utilizing the large conduction band offset (~3.5 eV) between $BaSnO_3$ and Al_2O_3. This high conduction band offset allows for a wide spectral range (from infrared to visible range) and tunability when used as a quantum well device. The deposition is done by molecular beam epitaxy and the heterostructures are characterized by Reflection High Energy electron diffraction (RHEED), X-ray Photoemission Spectroscopy (XPS) and Scanning Transmission Electron Microscopy (STEM) to confirm the quality and composition. This structure is a prototype implementation of the high-mobility-oxide quantum well design. We conducted Hall measurements to measure the mobility of the La doped BSO and optimize the doping process. We also conducted ellipsometry measurements of quantum wells with three different BSO thicknesses (3, 6, 12 unit cells) to observe the blue shift of the absorption edge of the heterostructure and confirm quantum confinement.

Both $BaSnO_3$ and $SrSnO_3$ have triggered significant interest in the area of transparent conductive oxides as they have large electron mobility and wide optical band gaps. Here, we propose an advanced quantum well structure design of $BaSnO_3$/STO taking advantage of the small effective mass of the $BaSnO_3$($0.19m_e$) which makes our quantum well much more tunable. The BSO/STO can create an asymmetrical quantum well from the BSO/air interface. The deposition process is done by MBE and the heterostructures are characterized by RHEED, XPS and STEM to confirm the quality and composition. This structure is a prototype implementation of the high mobility oxide quantum well design. We conducted Hall measurement to measure the mobility of

the La doped BSO and optimize the doping process. We also conducted ellipsometry measurements of quantum wells with three different BSO thicknesses (3, 6, 10uc) to observe the blue shift of the absorption edge of the heterostructure and to confirm quantum confinement. We were able to make the quantum well with up to the BSO layer just the contact with air and saw the blue shift from the ellipsometer with the varying BSO thickness which confirmed the quantum confinement of our heterostructure. In future, we could also use other barrier materials to make the conduction band offset between BSO and barrier material much larger which allows for wide spectral range (from infrared to visible range) and tunability when used as a quantum well device.

Chapter 2.1: Introduction

Alkaline earth stannate such as $BaSnO_3$(BSO) and $SrSnO_3$(SSO) have been widely studied due to their excellent mobility and optical transparence making them attractive as a transparent conductor and for applications in high-power electronic devices [5-14]. The wide band gap of a stannate is also suitable for building heterojunctions with large band offsets with certain materials. One can design quantum wells (QWs) by building heterostructures made of a thin layer of a "well material" between the two layers of another material with an even larger band gap which we call the "barrier material". The energy profile of the conduction band across the resulting heterostructure forms a quantum well for the electrons. The energy levels become discretized along the stacking direction to satisfy the Schrodinger equation boundary conditions in this confining potential. The allowed optical transitions can be controlled by the well thicknesses. Semiconductor quantum wells have been used as electro optical devices such as modulators [15], photodetectors [16], laser diodes [17], high performance transistors [18], integrated photonic devices [19] and quantum cascade lasers [20]. A number of quantum-well-based electro optical devices have previously been studied using GaAs/AlGaAs heterostructures [21-24]. However, the small

conduction band offset (much less than 1.0eV) limits the level of quantum confinement and only allows for the intersubband transition in a mid or far-infrared range. Metal-Oxide-based quantum wells can have a significantly larger conduction band offset than the semiconductor quantum wells, which allows for more energy levels to be confined in a well or to have a larger energy separation between the levels, which in turn allows for a larger operating energy range when used in a device. Although there has been another study of a wide bandgap quantum based on a LAO/STO heterostructure with a conduction band offset 2.3eV, the La doped STO has large effective mass resulting in a small energy spacing in the subbands [25]. This limits the tunability of the quantum well and negates the advantage of using the large band offset quantum well in the first place. On the other hand, BSO has a very low effective mass ($0.19m_0$)[26] due to the highly dispersive Sn 5s conduction band. This allows for much larger energy spacing and higher tunability. Quantum well (QW) utilizing BSO also has advantage that it can be directly integrated on silicon via an epitaxial $SrTiO_3$ buffer layer [27]. $BaSnO_3$ films can be readily doped n-type [28-30], allowing for our quantum well to be utilized as a unipolar intersubband (ISB) device.

The experiments showing the existence of QW states in heterostructures of transition metal oxides have been reported for $STO/SrVO_3/Vacuum$ heterostrucrtures [31] and a vacuum cleaved surface of STO [32], where the partially filled QW sub-bands were observed via angle-resolved photoemission spectroscopy (ARPES). There are relatively fewer reports of the large band offset quantum wells that allow mid-infrared intersubband absorption. Zhao et al. used ZnO/ZnMgO quantum wells to achieve mid-infrared intersubband absorption [33] and Ortmann et al. have successfully integrated LAO/STO superlattices on Si and demonstrated the ability to control intersubband absorption energy by changing the thickness of the STO well layers [29]. Additionally, Choi et al. have reported the blue shift in the absorption edge by ~0.39 eV as

STO quantum well thickness was reduced from ten to two-unit cells for the STO/LAO quantum well [34]. This demonstrated the tunability of the energy level of the first subband by varying the QW thickness.

A QW-based electro optical device may utilize the Stark effect in the intersubband absorption for the electro optical operation. This allows for a high-speed and low-power operation because the quantum-confined Stark effect requires very a short time to make energy transition and the electric-field-driven Stark effect does not require a current flow for operation [35]. Ortmann et al. have demonstrated that STO/LAO-based electro optic modulators had a switching energy in order of pJ/bit [36] which was competitive to the switching energy of some silicon Mach-Zehnder modulators [37-38]. Ortmann et al. have experimentally demonstrated the feasibility of using the STO/LAO system for Transition Metal Oxide (TMO) based QW devices by showing control of optically modulated intersubband transition and growing a thick multi quantum well (MQW) structure without deterioration in quality [39].

Oxide heterostructures including QWs have shown rich exotic properties at their interface, and they allow us to study exotic physics phenomena, as is the case of the highly conducting 2DEG found at the interface of the two insulating materials LAO and STO [40]. In $LaTiO_3/STO$ heterostructure, two-dimensional superconductivity was found at the interface [41] and the critical temperature was found to be tunable by electrostatic gating [42]. Wang et al. demonstrated through calculations that the AsO is an excellent candidate for two dimensional realistic materials that are able to realize room temperature quantum spin Hall effects [43]. Quantum confinement of strongly correlated electrons also allows the study of correlated Fermi liquid states in a reduced dimension. Yoshimatsu et al. have studied ultra-thin films of $SrVO_3$ on $Nb:SrTiO_3$ and they reported the creation and control of 2-dimensional electron-liquid states

[44]. The quantum well states in $SrVO_3$ showed the orbital-selective quantization and unusual band renormalization near the Fermi level. Yukawa et al. have studied the metal/Mott insulator quantum well state by resonant tunneling [45]. Additionally, the fabrication of novel TMO QW devices opens up new possibilities for advanced functionalities [46-47]. Jackson *et al.* showed interface-induced magnetism in $GdTiO_3/SrTiO_3$ and $SmTiO_3/SrTiO_3$ QWs [48]. Need et al. showed that, in $GdTiO_3/SrTiO_3$ quantum wells, the net ferromagnetism inherent to the Mott insulator $GdTiO_3$ matrix propagates into the nominally nonmagnetic STO QWs [49]. Choi et al. have reportd a $PbZrO_3/PbTiO_3$ QW with superior dielectric constant of 800 at a stacking period of 1 uc/1 uc (PZO_1/PTO_1) [50].

Our QW uses $BaSnO_3$ as the "well material" because of its low effective mass that allows for large subband energy spacing and high mobility. Carrier mobility is one of the most important characteristics of semiconductor material that determines the performance and speed of a device, in addition, BSO with its large band gap has potential for applications in high-power electronic devices [5-14].

Both $BaSnO_3$ and $SrSnO_3$ have been studied theoretically and experimentally, and particularly the stannate growth process has been examined [51-57]. Kim *et al.* [5] have reported very high mobility at room temperature for a Pulsed Laser Deposition (PLD) grown 4% La-doped BSO sample. Mobility in single crystal samples reached as high as 320 $cm^2/V•s$ while retaining their optical transparency. While in bulk this is the highest reported 300K mobility in perovskites, the mobility was still only up to 70 $cm^2/V•s$ in epitaxial films at that time. Later, Liu *et al.* [6] used first-principles calculations to explore the origin of the superior mobility in alkaline-earth stannate. Jalan's group has reported several studies of the stannate system. They used hybrid MBE with a metal-organic Sn source to grow stoichiometric BSO [7], which they

characterized with RHEED, STEM, electron energy-loss spectroscopy (EELS), and energy dispersive x-ray spectroscopy (EDX) to confirm the film quality, epitaxy, crystal structure, and composition. Conduction band offsets were also determined for BSO/STO and BSO/LAO interfaces to be 3.1 eV and 3.0 eV, respectively [8]. They also reported the adsorption-controlled BSO growth by hybrid MBE [9]. Films grown within this limited growth window are shown to yield La-doped BSO films with mobilities of 105 $cm^2/V•s$. Low mobility and charge compensation are induced in Ba- and Sn-deficient films, with a stronger Sn-deficiency dependence. They also analyzed the defect-driven localization crossover in La-doped SSO films [10]. It was pointed out that substrate-induced dislocations in the film strongly influence the electron phase coherence length, which causes a two-dimensional to three-dimensional weak localization crossover. They used epitaxial strain to control the SSO film phase and mobility [11] and achieved over 300% mobility enhancement at room temperature compared with the unstrained low-temperature orthorhombic polymorph. Stemmer's group also reported several MBE-grown BSO films with high mobility. They used $PrScO_3$ as a lattice-matched substrate and reported 150 $cm^2/V•s$ mobility at room temperature [12]. Structural images and band gap data of their stannate films were reported in a later publication [13]. Paik et al. have reported an adsorption-controlled BSO growth process by standard MBE [14]. BSO films grown on a $DyScO_3$ substrate demonstrated a 183 $cm^2/V•s$ mobility at room temperature and 400 $cm^2/V•s$ at 10 K.

In this chapter, we describe the MBE growth of a BSO/STO quantum well structure that takes advantage of the low effective mass of BSO to achieve a large energy separation of QW states. To design our QWs we compute the energy levels and the wavefunction using the Poisson-Schrodinger solver and monitor the crystallinity and the stoichiometry using *in-situ* RHEED and

ex-situ XPS. We successfully grew quantum wells with three different BSO thicknesses. We demonstrate the blue shift of the energy transition from the ground to the first excited state as the BSO thickness decreases using ellipsometry to demonstrate successful electronic QW confinement. We have performed a Hall measurement to measure the mobility of the La doped BSO and optimize the doping process.

Chapter 2.2: Quantum Well Design

To achieve a large conduction band offset quantum well with a large energy spacing to allow for high tunability and operating energy range, we employ a $BaSnO_3/STO/Al_2O_3$ QW structure. The conduction band offset of 0.49 eV between the STO (band gap of 3.27 eV) and BSO (band gap of 3.1 eV) is a part of the asymmetric QW, the confinement is provided by a large band gap of cubic alumina Al_2O_3 (7.6 eV). We deposit six-, eleven-, and sixteen-unit-cell-thick BSO layers on STO substrate using MBE. Cubic γ-Al_2O_3 is envisioned as a barrier

material, however, we couldn't find the epitaxial window to grow BSO on alumina and had to use a thin STO buffer to achieve epitaxy.

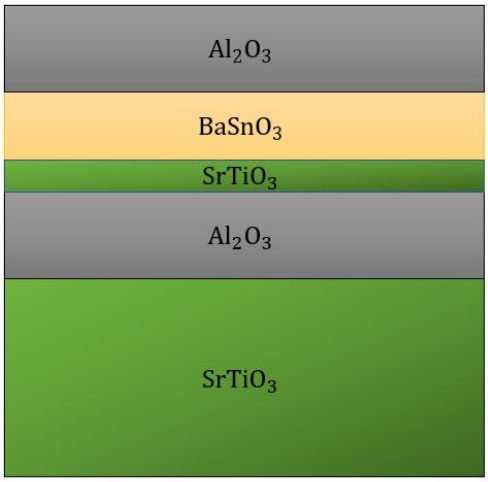

Figure 6: Schematic of the heterostructures. $Al_2O_3/STO/BaSnO_3/Al_2O_3$ quantum well is grown on STO (10×10×0.5mm) substate. Quantum well consists of ~4.5nm of Al_2O_3 layers, 2nm of STO (5uc) and varying thickness of the BSO layer.

The schematic of the proposed structure is shown in Figure 6 and band alignment of the stack determined by XPS is shown in Figure 7.

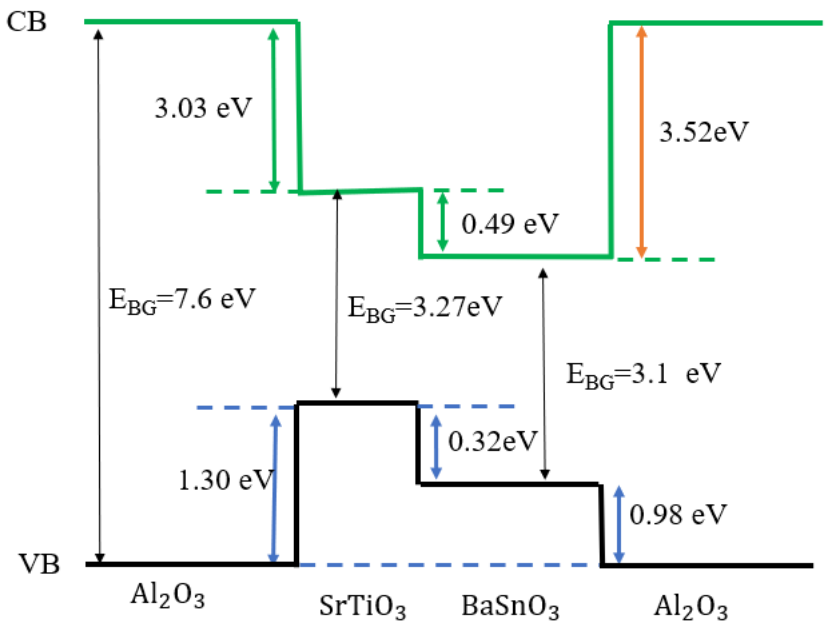

Figure 7: Band alignment of a single quantum well from the XPS data. The conduction band offset between BSO and $SrTiO_3$ is 0.49 eV and the conduction band offset between BSO and Al_2O_3 is 3.52 eV.

The valence band offsets (VBOs) marked in Figure 7 were extracted from the XPS measurements of various heterostructures consisting of alumina, BSO, and STO layers. First, we measure a core level and the valence band maximum (VBM) binding energies in alumina, STO, and BSO bulk-like films. Second, we measure the same core level binding energies in a BSO/STO a. Here, we use Sr *3d* in STO and Ba *4d* in BSO. For example, the VBO at the STO/BTO interface is calculated as follows:

$$VBO_{STO/BSO} = (E_{Sr\ 3d} - E_{VBM})_{STO} - (E_{Ba\ 4d} - E_{VBM})_{BSO} - (E_{Sr\ 3d} - E_{Ba\ 4d})_{STO/BSO}$$

With the same method, we get VBO_{STO/Al_2O_3} = 2.3 eV and VBO_{BSO/Al_2O_3} = 1 eV. We also know the experimental band gaps of each material, which allows one to obtain the conduction band offsets (CBO), as marked by green lines in Figure 7. We can see that the CBO for BSO and Al_2O_3 is very large at 3.52 eV.

Based on the CBO offsets and the well structure, we performed simulations using a Poisson-Schrodinger solver to determine the electronic structure of the QW.

3. POISSON SCHRODINGER SOLVER

Based on the CBO and the well width in this structure, we perform a simulation using a Poisson-Schrodinger solver to calculate the electron energy and wave function of the Al_2O_3/BSO QW. Calculating the energy levels helps us predict the possible intersubband transitions for the quantum well that we will grow to compare with the ellipsometry measurement. The well consists of 5-unit cells (uc) of STO and 3, 6, 10uc of BSO respectively and approximately 4-5nm of Al_2O_3 barriers on either side and the results are shown in Figure 8-10.

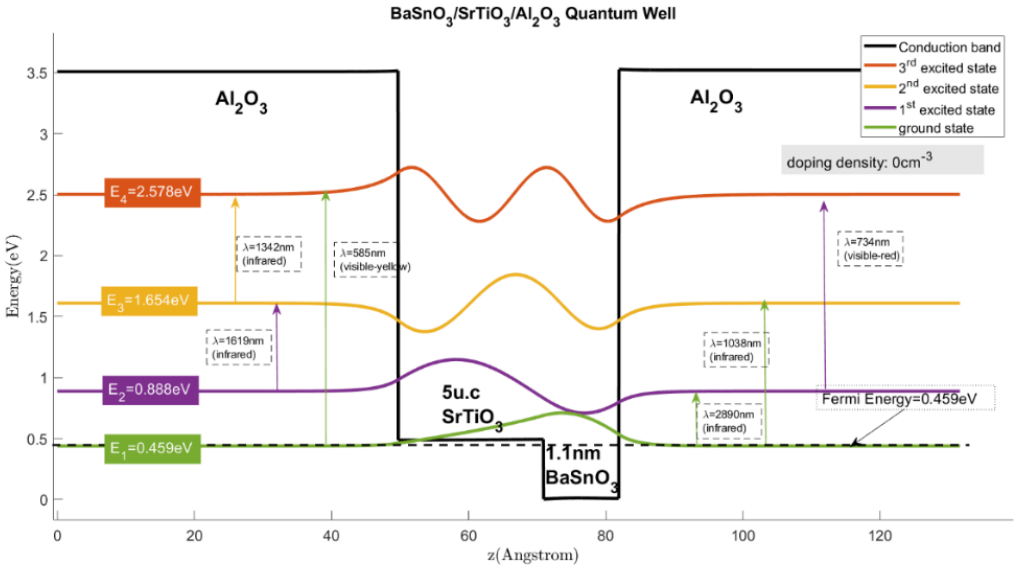

Figure 8: Simulation results for the energy states in a single QW. There are four energy levels in the quantum well. x-axis show the film's growth direction and y-axis show the conduction band energies in eV. The energy is set to be 0eV at the minimum of the BSO conduction band (at $BaSnO_3$ conduction band. Some of the intersubband transitions are shown with an arrow and corresponding wavelength. Doping density is 0 in the BSO layer. Effective mass used to calculate for the wavefunction is $0.4m_e$ for the Al_2O_3 layers and $4.2m_e$ for the STO layer and $0.19m_e$ for the BSO layer. Dielectric constant used to calculate for the wavefunction is 3.3 for Al_2O_3, 240 for $SrTiO_3$ and 20 for $BaSnO_3$. Wavefunction and energy levels of quantum well consisting of 3uc of BSO from the PS solver. There are 4 confined states in the well.

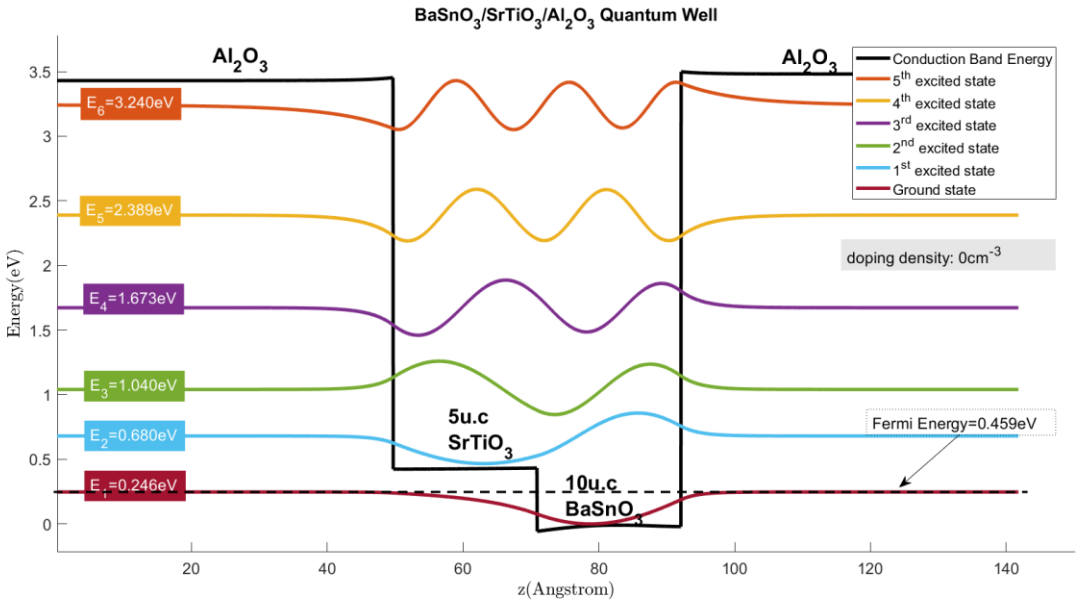

Figure 9: Simulation of a QW consisting of thick Al_2O_3 layer, 5uc of STO buffer layer and 6uc of BSO layer. There are 6 confined energy levels.

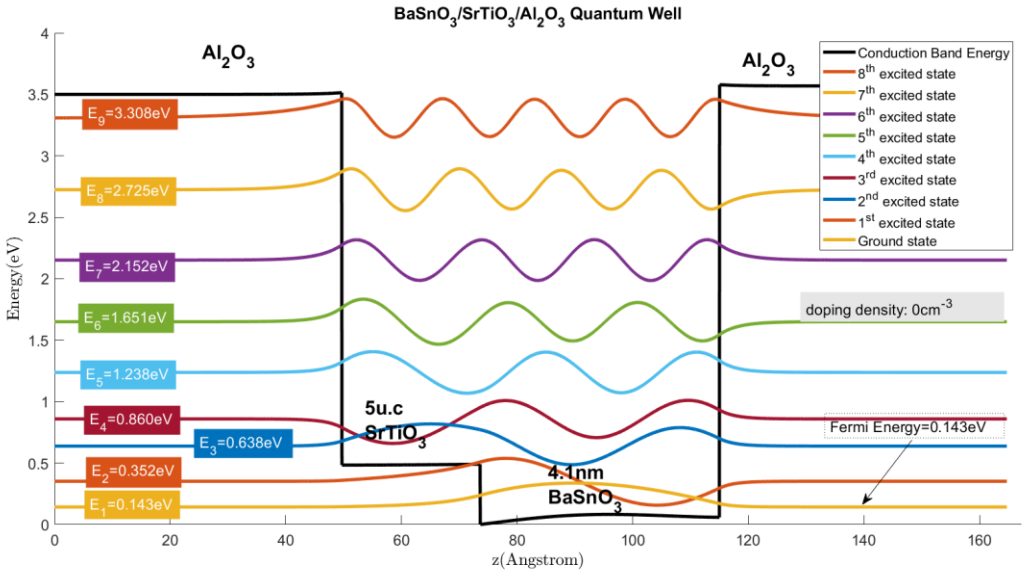

Figure 10: The wavefunction of a QW consisting of 10uc BSO. There are 9 confined states in the well.

Based on the energy levels in the well, we see that one can get transitions ranging from visible to infrared. This is a very promising QW structure with a wide range of absorption energy. The ellipsometry can measure transition down to 0.1eV, so QW we grow should have the transition from the ground to the first excited state larger than 0.1eV. We were able to predict the transition energies from the PS solver simulation and we found that the BSO thickness of 2-19uc is the range we can use to get the absorption measurement done. For BSO thickness of 20u.c and above, energy levels are too close together for the ellipsometry to measure. We used 3, 6 and 10uc of BSO layer for our study.

From the simulation, one can observe that quantum well consisting of the thicker BSO layer would confine more energy levels and the energy levels would be closer to each other. We would like to see quantum confinement by ellipsometry for different thickness of BSO. There is

an uncertainty in the predicted intersubband transition because the effective mass may vary depending on the doping [58], strain etc. [59] and band [60].

4. EXPERIMENTAL METHOD

The samples we study are $BaSnO_3/SrTiO_3$ quantum wells with undoped BSO thicknesses of eight-, twelve-, and sixteen-unit cell for the optical measurement. All the samples are grown on commercial $10 \times 10 \times 0.5mm^3$ single side polished STO (001) substrates. The STO substrate was degreased by acetone, isopropanol, and deionized water ultrasonically (5 minutes each), then exposed to UV/ozone to remove any organic impurities.

The growth was done by MBE with effusion cells for the metal evaporation and molecular oxygen used as the oxidant. To grow the γ-Al_2O_3, the cleaned STO substrates were introduced into a customized DCA 600 MBE system and were heated to substrate temperature of 700°C. The substrate was initially left at 700°C for 20-30 minutes to remove the surface contamination.

BSO has a decent lattice match with STO (-5.4% lattice mismatch) and grows well on it, and we can also use the STO/Si pseudo-substrate to integrate BSO on Si.

We deposited different thicknesses of BSO layer (3, 6, 10uc). Ba is evaporated from the effusion cell and Sn comes from an e-beam evaporator in the form of SnO_2. Using SnO_2 in the e-gun yields a 1-2×10^{-6} Torr base oxygen pressure during deposition, coming from the SnO_2 decomposition. Additional oxygen is needed to maintain a total oxygen pressure at 2-3×10^{-5} Torr to ensure that Sn is fully oxidized. We measure the flux of SnO_2 using QCM. The real Ba flux is also observed to decrease slightly when the oxygen pressure exceeds 10^{-5}Torr, likely due to source oxidation. This requires one to increase the Ba flux 1.2-1.3 times above the normal flux value to maintain the same atom arrival rate. The deposition temperature is maintained between 750-800 ˚C(we used 800 ˚C substrate temperature). Higher temperatures will result in Sn re-evaporation and failure to form the correct phase. At lower temperatures, BSO will not crystallize well. The

difficult part of using an e-gun for stannate deposition is the unstable flux. The SnO_2 flux decays too quickly, usually 20-40% over a 5-minute period when the rate is ~1 monolayer/min. To guarantee the crystal quality, the flux needs to be sufficiently stable to maintain the stoichiometric condition. Since we are using SnO_2 as Sn source, the total oxygen pressure is directly related to the Sn flux, and this has been verified to have a linear dependence by a flux measurement using a quartz crystal monitor. We use the real-time measured chamber pressure as a parameter to represent the Sn flux, and actively maintain the pressure by minor adjustments to the e-gun emission current to compensate the decaying flux during the entire deposition process. We successfully prepared QWs with the BSO layer thicknesses of 3, 6, and 10 uc.

Finally, we finish the quantum well by depositing 20 minutes of Al_2O_3 on top of the BSO layer at 700℃ and at oxygen partial pressure of 8×10^{-7}Torr. We weren't successful in growing Al_2O_3 to be crystalline when grown on top of the BSO, however, we made sure that the layers up to BSO maintained a good crystallinity. Amorphous Al_2O_3 still has a wide band gap that can perform as a barrier to the quantum well. Amorphous Al_2O_3 film has a relatively high dielectric permittivity and is regarded as promising gate dielectric for metal oxide semiconductor.

We grew each layer on different days, so after the growth of each layer, we cooled the substrate to 200℃ at a rate of 30℃/min and kept the oxygen pressure at the same level as was used during the growth until the substrate temperature cooled to below 300℃ to prevent oxygen vacancies in each layer.

To ensure the correct stoichiometry and good crystallinity, the growth of each layer was tested on a separate STO/Si substrate first. We did ex-situ x-ray reflectivity (XRR) measurements on the quantum well to find the thickness of each layer. We also did in situ XPS measurement to

check for the crystal quality and the stoichiometry and made sure that Ba and Sn had approximately a 1:1 ratio.

5. CHARACTERIZATION AND MEASUREMENT METHODS

The QW crystal structure was examined by RHEED, XRD, XRR and the optical properties were investigated via ellipsometry. We grew three different thicknesses of the BSO well layer

(3uc, 6uc, and 10uc) to investigate the effect of the well thickness on the energy levels. We monitored the crystallinity of each layer using *in-situ* RHEED during the growth.

Thickness-dependent X-ray reflectivity (XRR) measurements were performed on the QW heterostructure to determine the thickness of each layer. From the XRR measurement, we fitted the XRR data using GenX fitting program. From the fit, we extracted the approximate thickness of 3.51 nm of Al_2O_3, 2nm of STO, 1.04 nm of BSO and 3.51 nm of Al_2O_3 for the quantum well with 3 uc of BSO. For the quantum well with 6uc of BSO, the thickness was 4.0 nm of Al_2O_3, 2.1 nm of STO and 2.1 nm of BSO and 4 nm of Al_2O_3. For the quantum well with 10uc of BSO, the thickness was 4.1 nm of Al_2O_3, 2.4 nm of STO, 4.1 nm of BSO and 4.3 nm of Al_2O_3. The XRR fit was not perfect, because there were multiple layers and it was difficult to get a unique solution for the fit since there were so many parameters, so, instead we used the growth rate to estimate the thickness first and then did our best fit.

From the streaky RHEED pattern in Figure 11, we see that the overall crystallinity and the epitaxial quality of the film are very good up to the BSO layer.

(a)

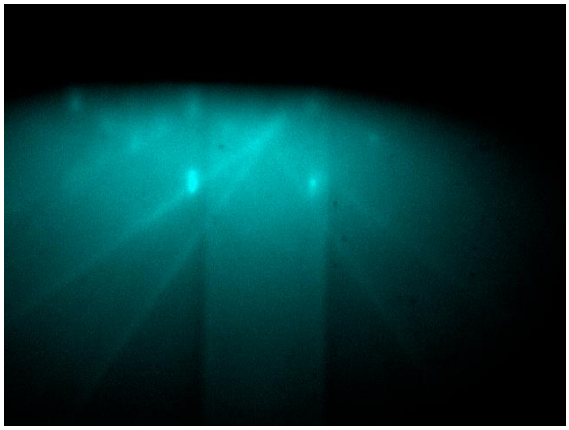

(b)

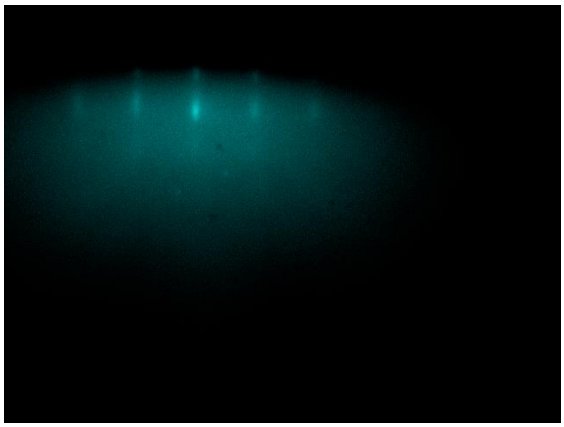

(c)

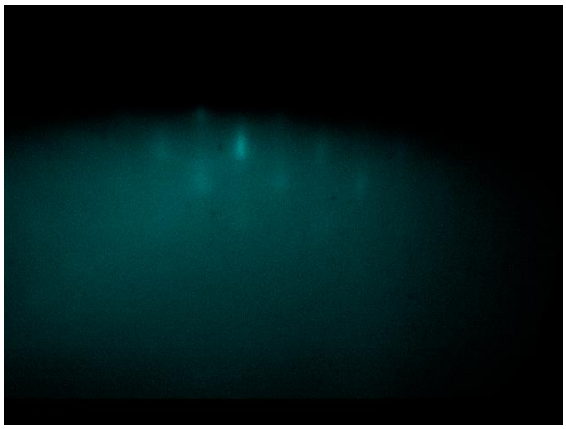

(d)

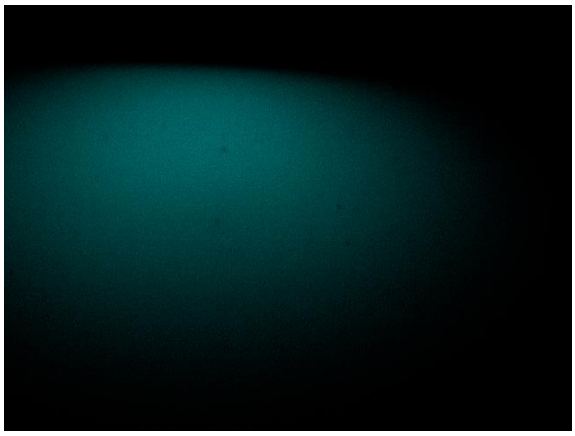

Figure 11: RHEED evolution from (a) 4.9nm Al_2O_3 on the STO substrate; (b) 5uc (2nm) STO buffer layer on the Al_2O_3 surface; (c) 16 uc (5.3nm) BSO on the STO surface; (d) 4.9nm amorphous Al_2O_3 on the BSO surface.

Additionally, we have performed the Hall measurements on the La-doped BSO (20nm thick) films on STO substrate ($10 \times 10 \times 0.5mm$) to optimize the doping process and measure the electron mobility. We also checked the stoichiometry of our La doped BSO using XPS.

For the first sample, XPS results showed that the ratio of Sn, Ba and La was 51.46%, 47.02% and 1.52%, respectively. The Hall measurement result showed that sheet resistance was 130.20 Ohms/sq and carrier concentration was $3.28 \times 10^{20}/cm^3$ and the mobility was $73.15 cm^2/Vs$.

For the second sample, by XPS, the ratio of Sn, Ba and La was 59.28%, 39.79% and 0.93%, respectively. The Hall measurement result showed that the sheet resistance was 159.59 ohms/sq and carrier concentration was $3.91 \times 10^{20}/cm^3$ and electron mobility was $59.06\ cm^2/Vs$.

We can use these carrier concentration values to control the doping of BSO for the La doped BSO quantum wells in the future.

Chapter 5.1: Valence band spectrum from XPS

We show the XPS measured valence band (VB) density of states of a BSO/STO /Al_2O_3 stack in Figure 12. This sample has 5 uc BSO on 3 uc STO on thick Al_2O_3 and shows a combination of STO VB and BSO VB features, the corresponding valence band densities of states are shown in Figures 13 and 14, respectively. The top of the valence band of STO is dominated by the p-states of non-bonded oxygen followed by the hybridized (bonded) oxygen-titanium band. Assuming the STO is slightly n-type (due to oxygen vacancies) the band gap appears to be 3.5 eV, slightly larger than in the bulk due to quantum confinement.

The top of the BSO valence band is dominated by the p-states of oxygen, a hybridized tin-oxygen band followed by the Ba p-state band are deeper and not shown in Figure 14.

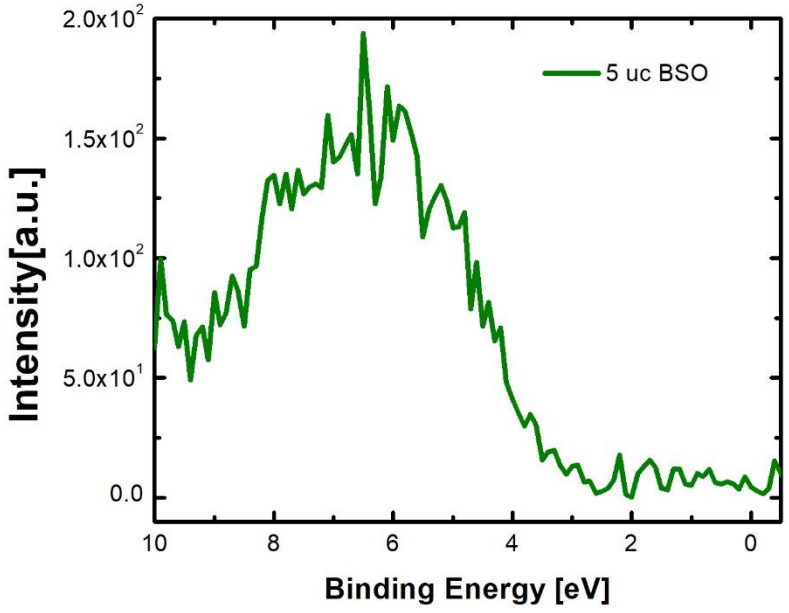

Figure 12: The valence band density of states of the 5 uc of BSO measured by XPS.

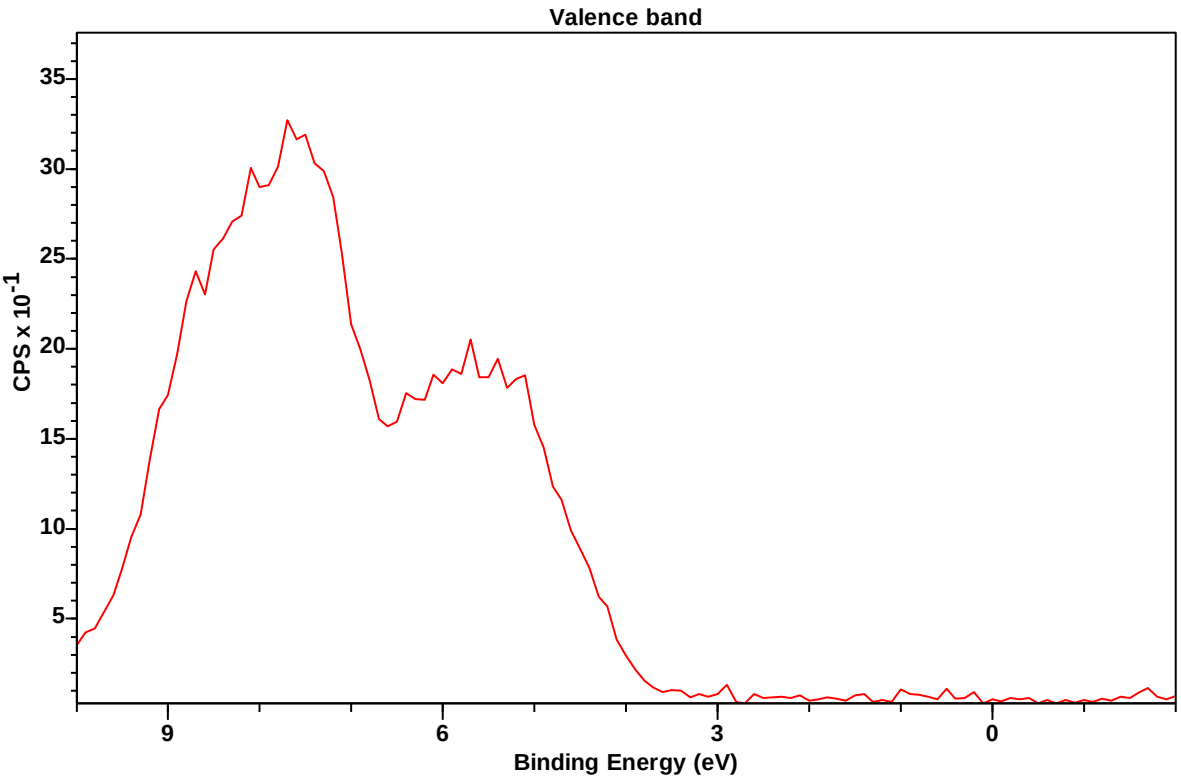

Figure 13: The valence band density of states of a thick, bulk-like STO film measured by XPS.

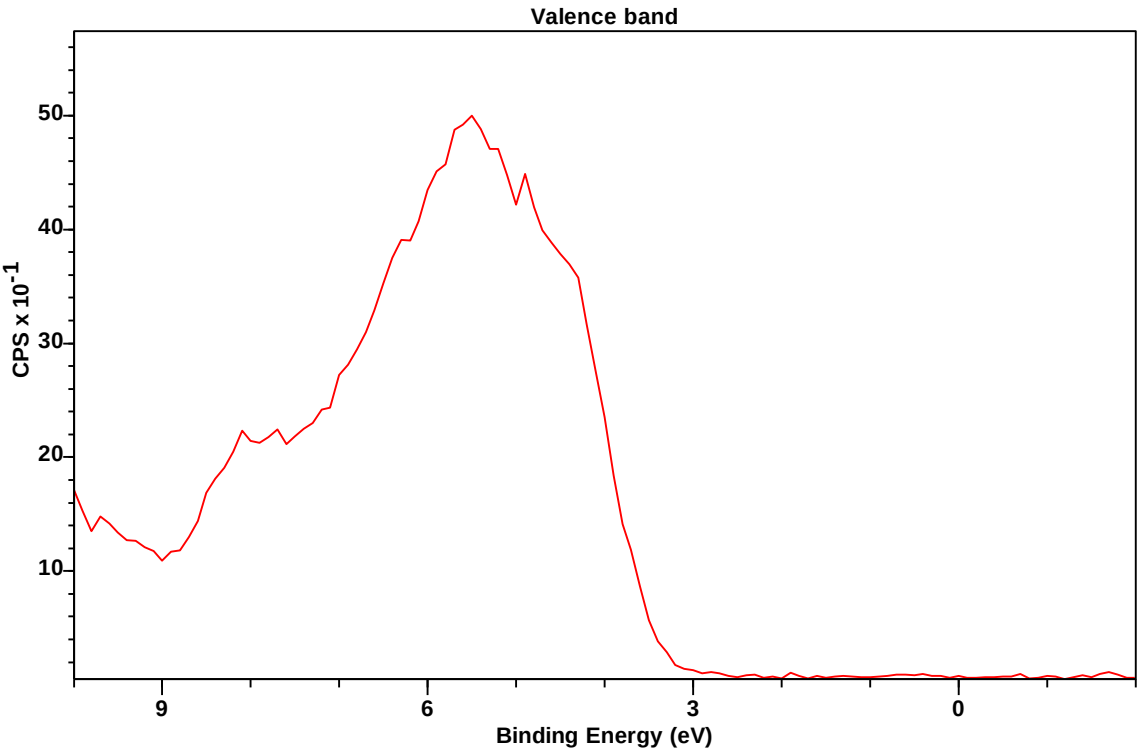

Figure 14: Valence band of a bulk-like BSO film measured by XPS.

Chapter 5.2: Ellipsometry measurements

We took ellipsometry measurements on a bare STO substrate, bulk $BaSnO_3$ on STO substrate, Al_2O_3 on STO substrate, $SrTiO_3$ on Al_2O_3 on STO substrate, $BaSnO_3$ on $SrTiO_3$ on Al_2O_3 on STO substrate, and Al_2O_3 on $BaSnO_3$ on $SrTiO_3$ on Al_2O_3 on STO substrate with three different BSO thicknesses (3,6,10uc). We have measured the quantum wells with ellipsometer at four different angles (60°, 65°, 70°, and 75°) before cleaning and after the cleaning (15min of deionized water ultrasonically and then 15min of isopropyl alcohol and then 30 minute of the ozone cleaning). We have used the thicknesses from the previous XRR measurements and fit the pseudo dielectric functions $<\varepsilon_1>$ and $<\varepsilon_2>$ by allowing the $BaSnO_3$ optical constant to be free.

We used the Tauc-Lorentz function for the $SrTiO_3$ and Cody-Lorentz function for the Al_2O_3 layer and 2 Tauc-Lorentz oscillators for the $BaSnO_3$ layer and we made sure that the error was low. We extracted the optical constants of the $BaSnO_3$ as a function of wavelength. From the optical constant, we used the Tauc plot to extract the E_g to compare it to the band gap of bulk BSO. We added a surface roughness layer to the model since there was the finite surface roughness of the films. We got E_g values of 3.692eV, 3.800eV, and 3.871eV for 10uc, 6uc, and 3uc of BSO, respectively, from the Tauc plot (see Figures 15-17). We do indeed see the blue shift of the absorption edge as we vary the BSO thickness since the E_g gets larger as the BSO thickness gets smaller which suggests that the first energy state in the quantum well gets higher as the thickness gets smaller. In Figure 18 we compare the experimental shift with the one predicted with the PS solver and find good agreement.

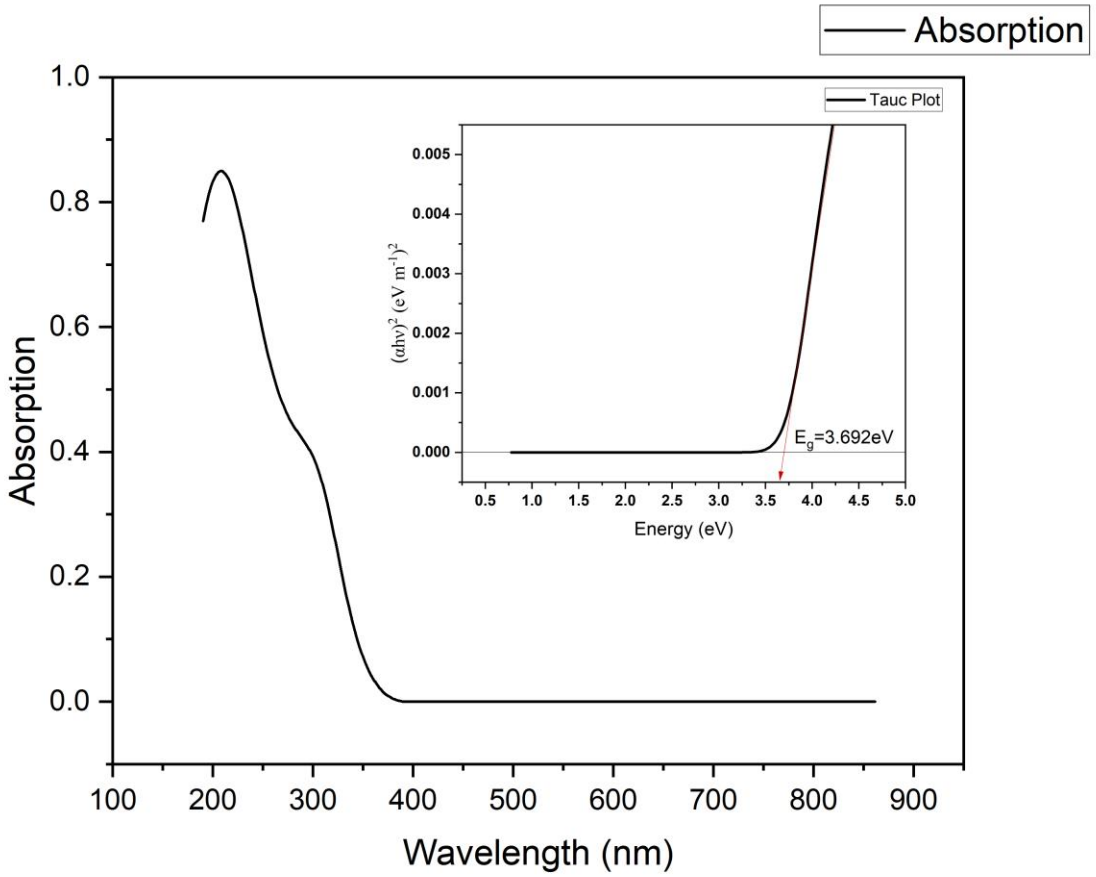

Figure 15: Absorption plot of a 10 uc-thick BSO QW (sample AM 66) and Tauc plot (insert on the right). The Tauc plot gives a gap of 3.692eV.

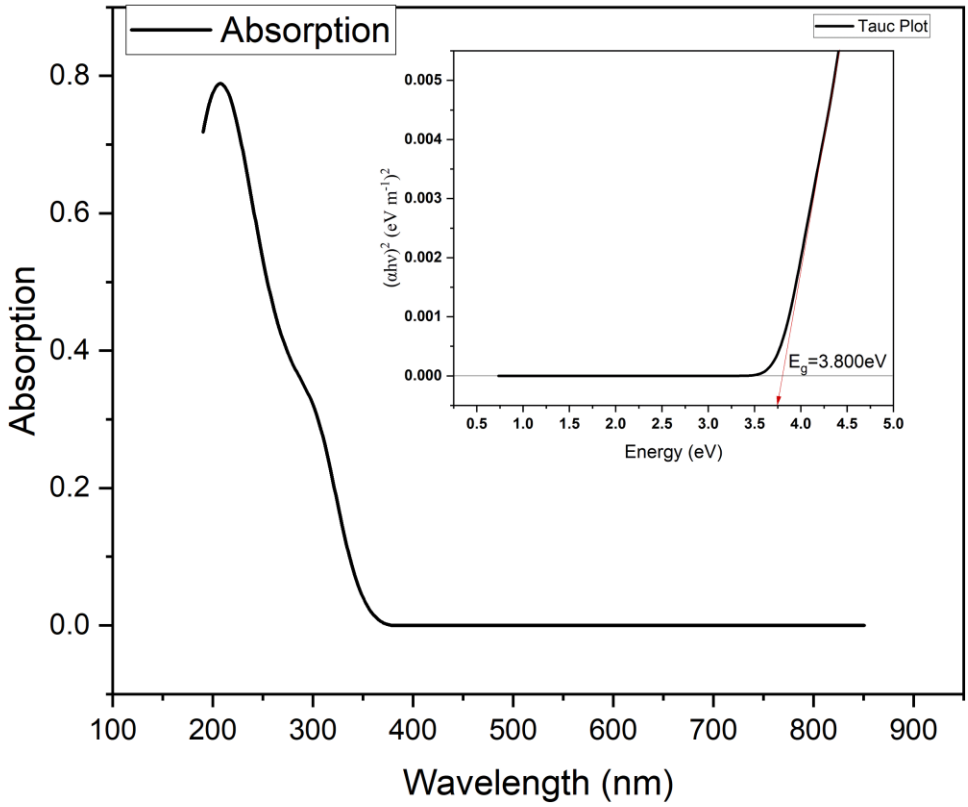

Figure 16: Absorption plot of a 6 uc-thick BSO QW (sample AM 67). The Tauc plot gives the gap of 3.8eV.

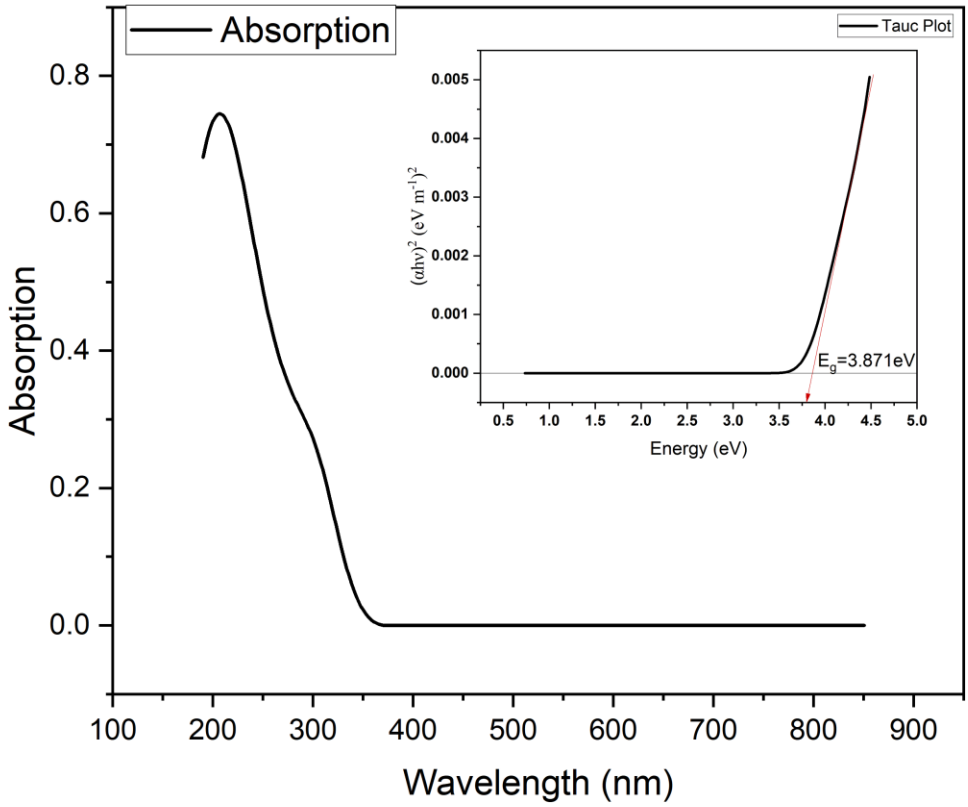

Figure 17: Absorbtion plot a 3 uc-thick BSO QW (sample AM 77). The Tauc plot gives a gap of 3.871eV.

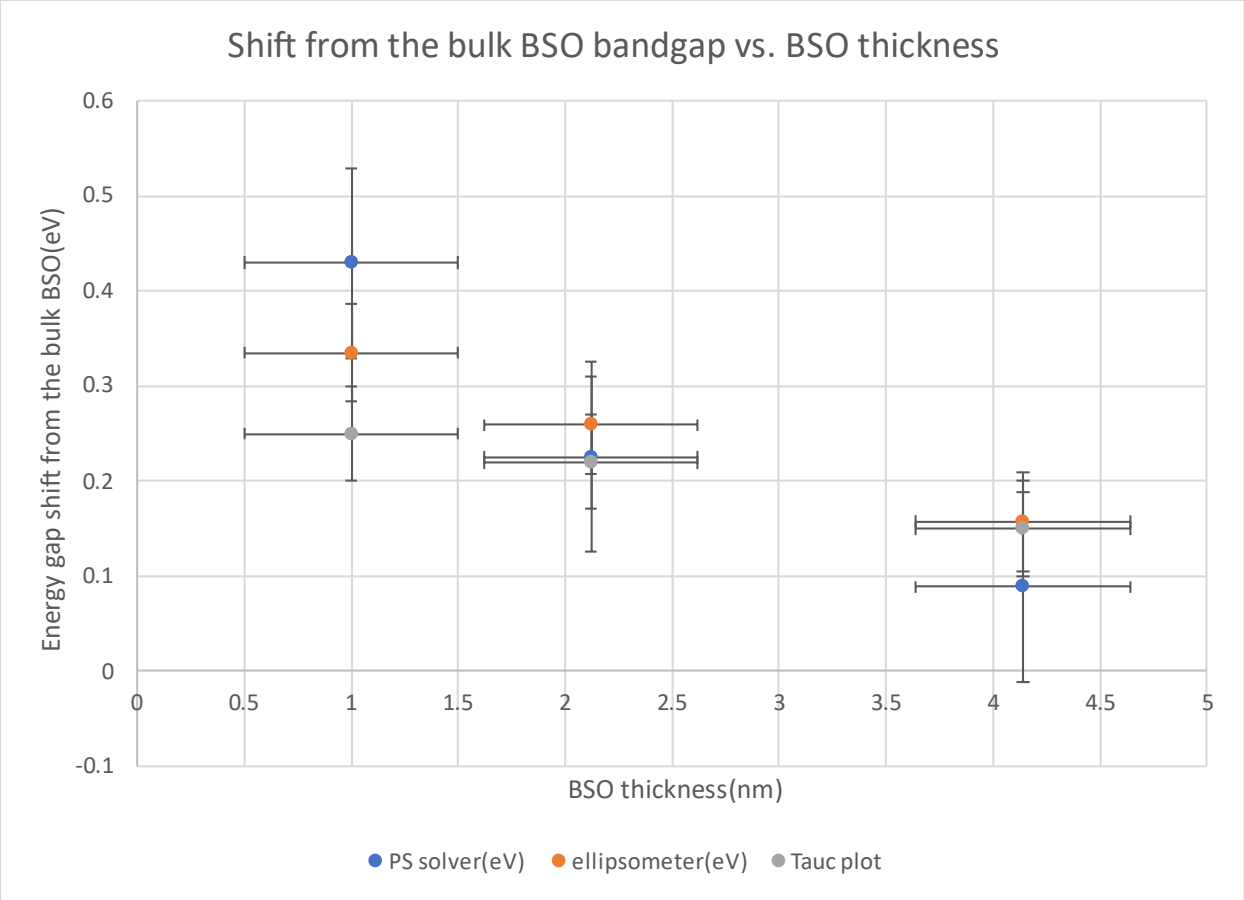

Figure 18: The band gap energy in eV vs. the BSO thickness in nm from the Tauc plot, PS solver and ellipsometer fit.

6. CONCLUSIONS

We have grown $BaSnO_3/SrTiO_3/Al_2O_3$ quantum wells using MBE. We utilized RHEED to check for the crystallinity of the film during the growth, cross-sectional STEM imaging to check for the interface quality and used in-situ XPS to check the stoichiometry and the band offset. Transport measurements of La-doped BSO films grown in our MBE were performed to optimize the doping process. We used ellipsometry to establish the blueshift of the absorption edge as the quantum well layer thickness is reduced for 8, 10, and 16uc BSO and find that the band gap shift agrees with the PS solver. This quantum well structure has a great potential for advanced quantum well devices once the process is optimized. In the future, we also can grow the quantum wells using MgO as the barrier because MgO has a wide bandgap of 7.8eV and there was a report that $BaSnO_3$ can grow directly on the MgO which eliminates the need for the STO buffer layer. MgO has a rock salt structure with lattice constant similar to that of BSO (4.1 Å for MgO and 4.116 Å for BSO). The work is a promising step towards achieving the large-offset-quantum-well for tunable energy intersubband absorption applications.

Acknowledgements

The work was supported by the Air Force Office of Scientific Research under grant FA9550-18-1-0053.

REFERENCES

1. Ichimiya, and P.I. Cohen, *Reflection High-Energy Electron Diffraction* (Cambridge University Press, Cambridge, 2004).
2. S. Hasegawa, in *Characterization of Materials* (John Wiley & Sons, Ltd, 2012), pp. 1–14.
3. J. A. Woollam Co.. *Ellipsometry Tutorial*, WWW Document, (jawoollam.com/resources)
4. K. Momma, and F. Izumi, "VESTA 3 for three-dimensional visualization of crystal, volumetric and morphology data," J. Appl. Cryst. **44**, 1272–1276 (2011).
5. H.J. Kim, U. Kim, Kim, T.H. Kim, H.S. Mun, B.-G. Jeon, K.T. Hong, W.-J. Lee, C. Ju, K.H. Kim, and K. Char, "High Mobility in a Stable Transparent Perovskite Oxide," Appl. Phys. Express **5**, 061102 (2012).
6. H.-R. Liu, J.-H. Yang, H.J. Xiang, X.G. Gong, and S.-H. Wei, "Origin of the superior conductivity of perovskite Ba(Sr)SnO_3," Appl. Phys. Lett. **102**, 112109 (2013).
7. Prakash, J. Dewey, H. Yun, J.S. Jeong, K.A. Mkhoyan, and B. Jalan, "Hybrid molecular beam epitaxy for the growth of stoichiometric BaSnO3," J. Vac. Sci. Technol. A **33**, 060608 (2015).
8. S.A. Chambers, T.C. Kaspar, A. Prakash, G. Haugstad, and B. Jalan, "Band alignment at epitaxial $BaSnO_3/SrTiO_3$(001) and $BaSnO_3/LaAlO_3$(001) heterojunctions," Appl. Phys. Lett. **108**, 152104 (2016).
9. Prakash, P. Xu, X. Wu, G. Haugstad, X. Wang, and B. Jalan, "Adsorption-controlled growth and the influence of stoichiometry on electronic transport in hybrid molecular beam epitaxy-grown $BaSnO_3$ films," J. Mater. Chem. C **5**, 5730–5736 (2017).
10. T. Wang, L.R. Thoutam, A. Prakash, W. Nunn, G. Haugstad, and B. Jalan, "Defect-driven localization crossovers in MBE-grown La-doped $SrSnO_3$ films," Phys. Rev. Mater. **1**, 061601 (2017).
11. T. Wang, A. Prakash, Y. Dong, T. Truttmann, A. Bucsek, R. James, D.D. Fong, J.-W. Kim, P.J. Ryan, H. Zhou, T. Birol, and B. Jalan, "Engineering SrSnO3 Phases and Electron Mobility at Room Temperature Using Epitaxial Strain," ACS Appl. Mater. Interfaces **10**, 43802–43808 (2018).
12. S. Raghavan, T. Schumann, H. Kim, J.Y. Zhang, T.A. Cain, and S. Stemmer, "High-mobility $BaSnO_3$ grown by oxide molecular beam epitaxy," APL Mater. **4**, 016106 (2016).
13. T. Schumann, S. Raghavan, K. Ahadi, H. Kim, and S. Stemmer, "Structure and optical band gaps of (Ba,Sr)SnO3 films grown by molecular beam epitaxy," J. Vac. Sci. Technol. A **34**, 050601 (2016).
14. H. Paik, Z. Chen, E. Lochocki, A. Seidner H., A. Verma, N. Tanen, J. Park, M. Uchida, S. Shang, B.-C. Zhou, M. Brützam, R. Uecker, Z.-K. Liu, D. Jena, K.M. Shen, D.A. Muller, and D.G. Schlom, "Adsorption-controlled growth of La-doped BaSnO3 by molecular-beam epitaxy," APL Mater. **5**, 116107 (2017).
15. D.R.P. Guy, N. Apsley, L.L. Taylor, S.J. Bass, and P.C. Klipstein, in *Quantum Well and Superlattice Physics* (SPIE, 1987), pp. 189–196.
16. B.F. Levine, "Quantum-well infrared photodetectors," J. Appl. Phys. **74**, R1–R81 (1993).

17. S. Nakamura, M. Senoh, S. Nagahama, N. Iwasa, T. Yamada, T. Matsushita, H.K.H. Kiyoku, and Y.S.Y. Sugimoto, “InGaN-Based Multi-Quantum-Well-Structure Laser Diodes,” Jpn. J. Appl. Phys. **35**, L74 (1996).
18. S. Datta, G. Dewey, J. Fastenau, M. Hudait, D. Loubychev, W. Liu, M. Radosavljevic, W. Rachmady, and R. Chau, IEEE Electron Device Lett. **28**, 685 (2007).
19. S. Abel, T. Stöferle, C. Marchiori, C. Rossel, M.D. Rossell, R. Erni, D. Caimi, M. Sousa, A. Chelnokov, B.J. Offrein, and J. Fompeyrine, “A strong electro-optically active lead-free ferroelectric integrated on silicon,” Nat. Commun. **4**, 1671 (2013).
20. J. Faist, F. Capasso, D.L. Sivco, C. Sirtori, A.L. Hutchinson, and A.Y. Cho, “Quantum Cascade Laser,” Science **264**, 553–556 (1994).
21. Dingle, W. Wiegmann, and C.H. Henry, “Quantum States of Confined Carriers in Very Thin $Al_xGa_{1-x}As$-GaAs-$Al_xGa_{1-x}As$ Heterostructures,” Phys. Rev. Lett. **33**, 827–830 (1974).
22. D. Chemla, D. Miller, P. Smith, A. Gossard, and W. Wiegmann, “Room temperature excitonic nonlinear absorption and refraction in GaAs/AlGaAs multiple quantum well structures,” IEEE J. Quantum Electron. **20**(3), 265–275 (1984).
23. M. Kohl, D. Heitmann, S. Tarucha, K. Leo, and K. Ploog, “Optical investigation of the exciton transfer between growth islands of different well widths in GaAs/$Al_xGa_{1-x}As$ quantum wells,” Phys. Rev. B **39**, 7736–7743 (1989).
24. H. Okamoto, “Semiconductor Quantum-Well Structures for Optoelectronics–Recent Advances and Future Prospects–,” Jpn. J. Appl. Phys. **26**, 315 (1987).
25. J.E. Ortmann, N. Nookala, Q. He, L. Gao, C. Lin, A.B. Posadas, A.Y. Borisevich, M.A. Belkin, and A.A. Demkov, “Quantum Confinement in Oxide Heterostructures: Room-Temperature Intersubband Absorption in $SrTiO_3$/$LaAlO_3$ Multiple Quantum Wells,” ACS Nano **12**, 7682–7689 (2018).
26. S. James Allen, S. Raghavan, T. Schumann, K.-M. Law, and S. Stemmer, “Conduction band edge effective mass of La-doped $BaSnO_3$,” Appl. Phys. Lett. **108**(25), 252107 (2016).
27. W. Wunderlich, H. Ohta, and K. Koumoto, “Enhanced effective mass in doped $SrTiO_3$ and related perovskites,” Physica B: Condens. Matter **404**, 2202–2212 (2009).
28. Biswas, N. Li, M.H. Jung, Y.W. Lee, J.S. Kim, and Y.H. Jeong, “La doped $SrTiO_3$ thin films on $SrLaAlO_4$ (001) as transparent conductor,” J. Appl. Phys. **113**, 183711 (2013).
29. J. Son, P. Moetakef, B. Jalan, O. Bierwagen, N.J. Wright, R. Engel-Herbert, and S. Stemmer, “Epitaxial $SrTiO_3$ films with electron mobilities exceeding 30,000 cm2 V−1 s−1,” Nat. Mater. **9**, 482–484 (2010).
30. M. Choi, A. B. Posadas, C. A. Rodriguez, A. O'Hara, H. Seinige, A. J. Kellock, M. M. Frank, M. Tsoi, S. Zollner, V. Narayanan, and A. A. Demkov, "Structural, optical, and electrical properties of strained La-doped $SrTiO_3$," J. Appl. Phys. **116**, 043705 (2014).
31. K. Yoshimatsu, K. Horiba, H. Kumigashira, T. Yoshida, A. Fujimori, and M. Oshima, “Metallic Quantum Well States in Artificial Structures of Strongly Correlated Oxide,” Science **333**, 319–322 (2011).
32. A.F. Santander-Syro, O. Copie, T. Kondo, F. Fortuna, S. Pailhès, R. Weht, X.G. Qiu, F. Bertran, A. Nicolaou, A. Taleb-Ibrahimi, P. Le Fèvre, G. Herranz, M. Bibes, N.

Reyren, Y. Apertet, P. Lecoeur, A. Barthélémy, and M.J. Rozenberg, “Two-dimensional electron gas with universal subbands at the surface of $SrTiO_3$,” Nature **469**, 189–193 (2011).
33. K. Zhao, G. Chen, B.-S. Li, and A. Shen, “Mid-infrared intersubband absorptions in ZnO/ZnMgO multiple quantum wells,” Appl. Phys. Lett. **104**, 212104 (2014).
34. M. Choi, C. Lin, M. Butcher, C. Rodriguez, Q. He, A. Posadas, A. Y. Borisevich, S. Zollner, and A. A. Demkov, "Quantum confinement in transition metal oxide quantum wells," Appl. Phys. Lett. **106**, 192902 (2015).
35. A. Ohtomo, and H.Y. Hwang, “A high-mobility electron gas at the $LaAlO_3/SrTiO_3$ heterointerface,” Nature **427**, 423–426 (2004).
36. J. Biscaras, N. Bergeal, A. Kushwaha, T. Wolf, A. Rastogi, R.C. Budhani, and J. Lesueur, “Two-dimensional superconductivity at a Mott insulator/band insulator interface $LaTiO_3/SrTiO_3$,” Nat Commun **1**, 89 (2010).
37. J. Biscaras, N. Bergeal, S. Hurand, C. Grossetête, A. Rastogi, R.C. Budhani, D. LeBoeuf, C. Proust, and J. Lesueur, “Two-Dimensional Superconducting Phase in $LaTiO_3/SrTiO_3$ Heterostructures Induced by High-Mobility Carrier Doping,” Phys. Rev. Lett. **108**, 247004 (2012).
38. Y. Wang, W. Ji, C. Zhang, P. Li, S. Zhang, P. Wang, S. Li, and S. Yan, “Two-dimensional arsenene oxide: A realistic large-gap quantum spin Hall insulator,” Appl. Phys. Lett. **110**, 213101 (2017).
39. K. Yoshimatsu, K. Horiba, H. Kumigashira, T. Yoshida, A. Fujimori, and M. Oshima, “Metallic Quantum Well States in Artificial Structures of Strongly Correlated Oxide,” Science **333**, 319–322 (2011).
40. R. Yukawa, M. Kobayashi, T. Kanda, D. Shiga, K. Yoshimatsu, S. Ishibashi, M. Minohara, M. Kitamura, K. Horiba, A.F. Santander-Syro, and H. Kumigashira, “Resonant tunneling driven metal-insulator transition in double quantum-well structures of strongly correlated oxide,” Nat. Commun. **12**, 7070 (2021).
41. J.D. Hwang, C.I. Jiang, and S.B. Hwang, “P-NiO/n-ZnO heterojunction photodiodes with an MgZnO/ZnO quantum well insertion layer,” Mater. Sci. Semicond. Process. **105**, 104711 (2020).
42. P. Sikam, R. Thirayatorn, P. Moontragoon, T. Kaewmaraya, V. Amornkitbamrung, and Z. Ikonic, “The quantum confined Stark effect in N-doped ZnO/ZnO/N-doped ZnO nanostructures for infrared and terahertz applications,” Nanotechnology **31**, 445207 (2020).
43. M.W. Klein, C. Enkrich, M. Wegener, and S. Linden, “Second-Harmonic Generation from Magnetic Metamaterials,” Science **313**(5786), 502–504 (2006).
44. N. Feth, S. Linden, M.W. Klein, M. Decker, F.B.P. Niesler, Y. Zeng, W. Hoyer, J. Liu, S.W. Koch, J.V. Moloney, and M. Wegener, “Second-harmonic generation from complementary split-ring resonators,” Opt. Lett., OL **33**, 1975–1977 (2008).
45. W. Fan, S. Zhang, K.J. Malloy, S.R.J. Brueck, N.C. Panoiu, and R.M. Osgood, “Second harmonic generation from patterned GaAs inside a subwavelength metallic hole array,” Opt. Express, OE **14**, 9570–9575 (2006).
46. D.S. Chemla, T.C. Damen, D.A.B. Miller, A.C. Gossard, and W. Wiegmann, “Electroabsorption by Stark effect on room-temperature excitons in GaAs/GaAlAs multiple quantum well structures,” Appl. Phys. Lett. **42**, 864–866 (1983).

47. J.E. Ortmann, M.A. Duncan, and A.A. Demkov, “Designing near-infrared electro-optical devices from the $SrTiO_3/LaAlO_3$ materials system,” Opt. Mater. Express, OME **9**, 2982–2993 (2019).
48. L. Liao, D. Samara-Rubio, M. Morse, A. Liu, D. Hodge, D. Rubin, U.D. Keil, and T. Franck, “High speed silicon Mach-Zehnder modulator,” Opt. Express, OE **13**, 3129–3135 (2005).
49. W.M.J. Green, M.J. Rooks, L. Sekaric, and Y.A. Vlasov, “Ultra-compact, low RF power, 10 Gb/s silicon Mach-Zehnder modulator,” Opt. Express, OE **15**, 17106–17113 (2007).
50. J. E. Ortmann, N. Nookala, Q. He, L. Gao, C. Lin, A. B. Posadas, A. Y. Borisevich, M. A. Belkin, and A. A. Demkov, "Quantum confinement in oxide heterostructures: Room-temperature intersubband absorption in $SrTiO_3/LaAlO_3$ multiple quantum wells," ACS NANO **12**, 7682 (2018).
51. F.B.P. Niesler, N. Feth, S. Linden, J. Niegemann, J. Gieseler, K. Busch, and M. Wegener, “Second-harmonic generation from split-ring resonators on a GaAs substrate,” Opt. Lett., OL **34**, 1997–1999 (2009).
52. J. Lee, M. Tymchenko, C. Argyropoulos, P.-Y. Chen, F. Lu, F. Demmerle, G. Boehm, M.-C. Amann, A. Alù, and M.A. Belkin, “Giant nonlinear response from plasmonic metasurfaces coupled to intersubband transitions,” Nature **511**, 65–69 (2014).
53. M. Gurnick, and T. DeTemple, “Synthetic nonlinear semiconductors,” IEEE J. Quantum Electron. **19**, 791–794 (1983).
54. M.M. Fejer, S.J.B. Yoo, R.L. Byer, A. Harwit, and J.S. HarrisJr., “Observation of extremely large quadratic susceptibility at 9.6--10.8 μm in electric-field-biased AlGaAs quantum wells,” Phys. Rev. Lett. **62**, 1041–1044 (1989).
55. E. Rosencher, and Ph. Bois, “Model system for optical nonlinearities: Asymmetric quantum wells,” Phys. Rev. B **44**, 11315–11327 (1991).
56. P. Boucaud, F.H. Julien, D.D. Yang, J. Lourtioz, E. Rosencher, P. Bois, and J. Nagle, “Detailed analysis of second-harmonic generation near 10.6 μm in GaAs/AlGaAs asymmetric quantum wells,” Appl. Phys. Lett. **57**, 215–217 (1990).
57. P. Boucaud, F.H. Julien, D.D. Yang, J.-M. Lourtioz, E. Rosencher, and P. Bois, “Saturation of second-harmonic generation in GaAs–AlGaAs asymmetric quantum wells,” Opt. Lett., OL **16**, 199–201 (1991).
58. W. Wunderlich, H. Ohta, and K. Koumoto, “Enhanced effective mass in doped SrTiO3 and related perovskites,” Physica B: Condens. Matter **404**, 2202–2212 (2009).
59. A. Janotti, D. Steiauf, and C.G. Van de Walle, “Strain effects on the electronic structure of SrTiO3: Toward high electron mobilities,” Phys. Rev. B **84**, 201304 (2011).
60. A.F. Santander-Syro, O. Copie, T. Kondo, F. Fortuna, S. Pailhès, R. Weht, X.G. Qiu, F. Bertran, A. Nicolaou, A. Taleb-Ibrahimi, P. Le Fèvre, G. Herranz, M. Bibes, N. Reyren, Y. Apertet, P. Lecoeur, A. Barthélémy, and M.J. Rozenberg, “Two-dimensional electron gas with universal subbands at the surface of SrTiO3,” Nature **469**, 189–193 (2011).